Tectonophysics 659 (2015) 183–196

Contents lists available at ScienceDirect

Tectonophysics

journal homepage: www.elsevier.com/locate/tecto

The geometry of the Chilean continental wedge: Tectonic segmentation of subduction processes off Chile

Andrei Maksymowicz *

Departamento de Geofisica, Facultad de Ciencias Físicas y Matemáticas, Universidad de Chile, Santiago, Chile

ARTICLE INFO

Article history:
Received 30 October 2014
Received in revised form 22 July 2015
Accepted 12 August 2015
Available online 20 August 2015

Keywords:
Subduction
Wedge tectonics
Non-Cohesive Coulomb wedge theory
Seismic
Earthquakes

ABSTRACT

Based on high-resolution bathymetry and geophysical observations, the precise continental wedge geometry along the Chilean margin is analyzed. The data show complex patterns in continental wedge geometry that challenge the most frequently used classification methodology for the convergent margin tectonics. A detailed modeling of the parameters involved in the Non-Cohesive Coulomb Wedge theory reveals a tectonic latitudinal segmentation of the Chilean offshore subduction zone. This segmentation is characterized by a sequence of broad segments with different basal effective friction coefficient and/or internal fluid pressure conditions, which are limited by the presence of bathymetric oceanic highs, fracture zones and Peninsulas. The results suggest a general increase of the fluid pressure inside the continental wedge north of 33°S, which is interpreted as a result of a more pervasive fracturing due to tectonic erosion at the base and within the continental wedge. The tectonic segmentation proposed here shows a close spatial relation with the short-term deformation process associated to the coseismic ruptures of large earthquakes in the Chilean margin.

1. Introduction

The geometry and deformation styles observed in the continental wedges reveal a high variability of tectonic conditions along the convergent margins. In the case of accretionary margins, the turbiditic/pelagic trench sediment sequence is frontally obducted to the upper plate forming the frontal accretionary prism (Clift and Vannucchi, 2004; Lallemand et al., 1994, and references therein), which can be described as a particular case of a submarine fold-and-thrust-belt, where the interplate boundary corresponds to the basal decollement and where the backstop (the interface between the deformed sediments and the comparably rigid continental basement) works as an indenter (Dahlen, 1984). In contrast, the erosive margins are characterized by the lack of sediments at the trench and the absence of a frontal accretionary prism. The small sedimentary cover and the roughness of the subducted plate favor the material removal from the frontal portion and from the base of the continental wedge, resulting in the gravitational collapse and the associated normal faulting of the continental wedge (Ranero et al., 2006; Clift and Vannucchi, 2004; Lallemand et al., 1994, and references therein).

Several morphological and geodynamic parameters are relevant to characterize the tectonic state of convergent margins. Analyzing a set of margins in the Circum-Pacific area, Lallemand et al. (1994) identified the increases of the: convergence rate, slope angle (α), shallow subduction angle (β), and the roughness of the subducted slab as parameters that favor tectonic erosion. In contrast, the increase of the sediment thickness at the trench favors tectonic accretion. Clift and Vannucchi (2004) confirmed the importance of the convergence rate and the sediment thickness at the trench to classify the margins worldwide in terms of their accretionary or erosive style. Lallemand et al. (1994), propose a tectonic classification of the convergent margins in an α vs. β diagram, defining three clusters: Non-accretionary, Intermediate and Accretionary. This graphical analysis derivates from the Non-Cohesive Coulomb Wedge theory (NCCW), where the continental wedge is approximated by a homogeneous tapered body defined by constant angles α and β (Dahlen et al., 1984; Zhao et al., 1986). Several authors have adopted the classification of Lallemand et al. (1994), as well as the simple NCCW model to infer physical properties (friction coefficients and/or fluid pressure) for specific segments of subduction zones (MacKay, 1995; Kopp and Kukowski, 2003; Polonia et al., 2007; Cubas et al., 2013a,b; among other authors).

The geometry and the internal deformation of the continental wedge is a cumulative process that involves short-term events such as landward fault rotation, generation of out-of-sequence thrusts, changes on the convergence rate, and episodic intervals of erosion due to the subduction of bathymetric highs or a decrease in the sediment trench fill (Dominguez et al., 2000; Gutscher et al., 1996; Maksymowicz et al., 2012; Simpson, 2010). Thus, the tectonic style in convergent margins can be classified in a broad spectrum of conceptual models, whose end-members are the accretionary margins and the erosive margins. Due to its remarkable latitudinal variability on the trench sedimentation, convergence rate and subducted oceanic features, the Chilean

* Blanco Encalada 2002, Santiago, Chile.

http://dx.doi.org/10.1016/j.tecto.2015.08.007
0040-1951/

margin is a natural laboratory to study the sensibility of the continental wedge tectonics in response to variations of physical and rheological parameters, and can provide new insights about the meaning of the NCCW theory and the α vs.β classification at different spatial and time scales.

In this work, I show by means of the NCCW theory that variations of the tectonic style along the Chilean margin correlate with structures revealed in elevation and magnetic regional data.

2. Tectonic setting

The Chilean margin is characterized by the interaction of the Nazca, Antarctic, South America and Scotia plates (Fig. 1). Between ~18°S and 46.5°S, the rapid subduction of the Nazca Plate under South America at a convergence rate >66 km/Myr has been slightly oblique to the trench during the last ~25 Myr (Angermann et al., 1999; Cande and Leslie, 1986), and it determines a general compressive tectonics in the zone. This segment of the Chilean margin has generated several of the largest megathrust earthquakes recorded and historically reported (e.g. Valdivia1960 Mw9.6, Maule 2010 Mw8.8, Iquique 2014 ~Mw8.1, Valparaiso 1730 ~M8.7, Iquique 1877 ~M8.5, Vallenar 1922 ~M8.4; see Comte and Pardo, 1991; Beck et al.,1998; Cisternas et al., 2005; Ruegg et al.,2009; Bilek,2010; Moreno et al., 2012; Lay et al., 2014, and references therein).

Between 46.5°S (latitude of Chile Triple Junction, CTJ) and ~52°S the margin is characterized by the subduction of the Antarctica oceanic plate beneath South America with a low convergence rate of ~20 km/Myr. The Antarctica–South America convergence direction has been perpendicular to the trench from at least the early Eocene (Cande and Leslie, 1986). South of ~52°S, the strike-slip boundary between South America and Scotia plates accommodates part of the convergence resulting in a convergence rate for the Antarctica–Scotia subduction of about 13 km/Myr (Thomas et al., 2003).

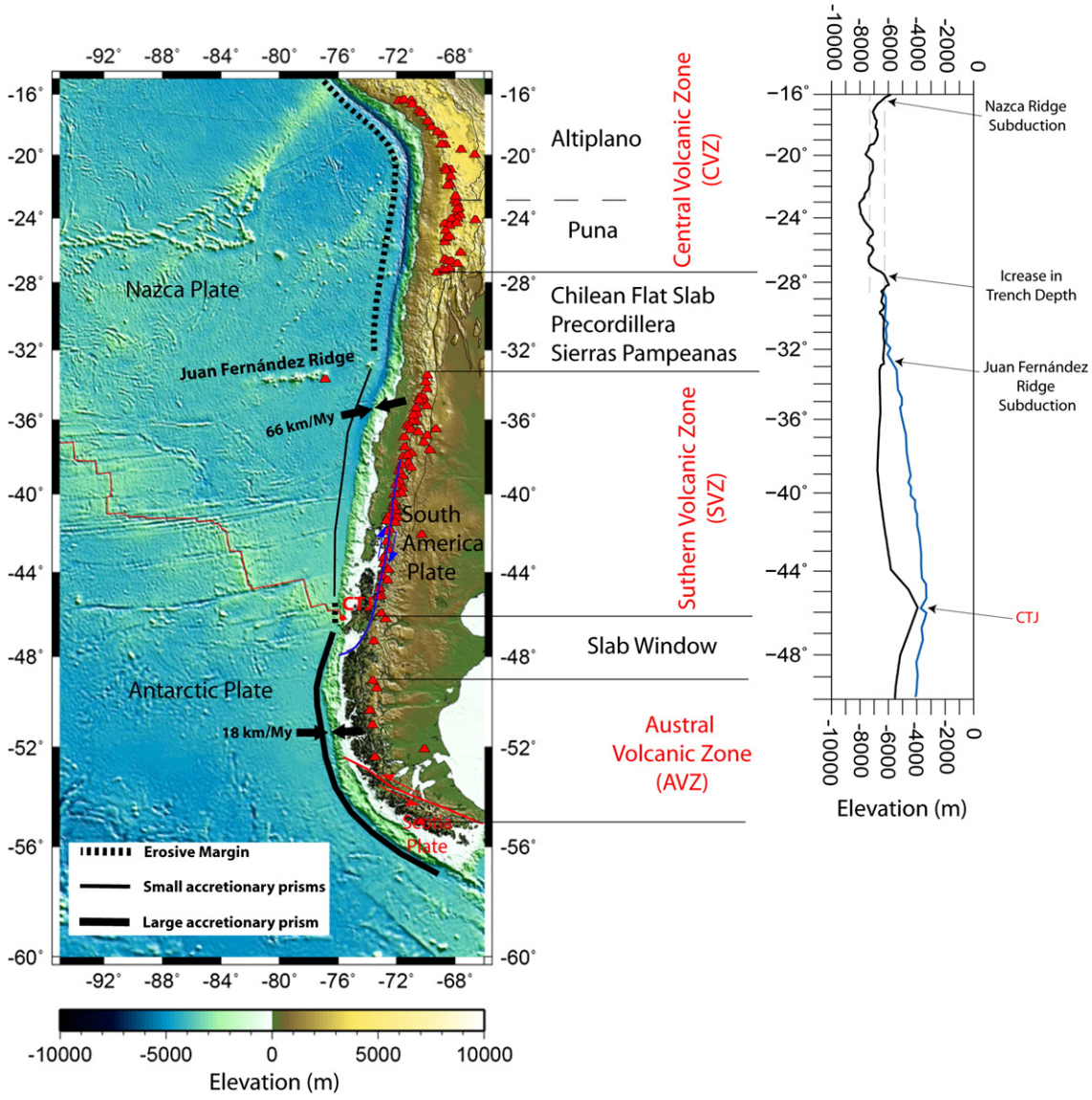

Fig. 1. Present day tectonic setting of the Chilean margin. The first order tectonic segmentation of the Chilean continental wedge is shown over an elevation map of the Chilean Margin. Red triangles correspond to the location of Quaternary volcanoes and the blue line corresponds to the intra-crustal Liquiñe-Ofqui fault system. CTJ indicates the location of the Chile Triple Junction. The limits of the major tectonic segments of the Andes and Quaternary volcanic zones are also indicated. Black line in the right panel shows the elevation of the slab at the Peru–Chile trench as a function of latitude (modified from Contereras-Reyes and Osses (2010)), and the blue line corresponds to the seafloor elevation at the same latitudes. The difference between these curves is the sedimentary thickness of the Peru–Chile trench.

The kinematics of the Antarctica–Nazca–South America spreading center (Chile Rise) referred to South America, caused a northward migration of the CTJ since ~14 Ma, from ~53°S to its current position at 46.5°S. Thus, the length of the Antarctica–South America subduction zone has increased in this time period (Cande and Leslie, 1986).

Fig. 1 shows that almost 50% of the Chilean continental forearc corresponds to the marine shelf and continental wedge, which makes the study of these structures relevant in order to obtain a more complete view of the Chilean subduction zone. Mainly by interpretation of seismic reflection profiles and wide-angle refraction seismic profiles, a first order segmentation in the tectonic style of the Chilean continental wedge has been proposed: (1) the northern segment, extended between Arica and the Juan Fernández Ridge subduction point (JFR), corresponds to an erosive margin conditioned by the low trench sedimentation and the high Nazca–South America convergence rate. This segment shows normal failure, absence of the accretionary prism, and a steep slope (Contreras-Reyes et al., 2012; Contreras-Reyes et al., 2014; Ranero et al., 2006; Sallares and Ranero, 2005). (2) Between the JFR and the CTJ, a frontal prism relatively small in size (<50 km width) is associated with a high trench fill, but consistent with the high Nazca–South America convergence rate. The main deformation style of the continental wedge can be defined as west vergent reverse faulting of generally low angle (Bangs and Cande, 1997; Contreras-Reyes et al., 2008, 2010; Diaz-Naveas, 1999; Moscoso et al., 2011; Scherwath et al., 2009; Zelt, 1999). (3) Southward of the CTJ, the margin presents a wide accretionary prism (>50 km) in response to the low Antarctica–South America convergence rate (~20 km/Myr) and the high trench fill. In this southern segment, the deformation style is characterized by a general west vergent reverse high angle faulting associated to quasi-symmetric folding (Polonia et al., 2007; Ranero et al., 2006). (4) Locally, the subduction of the Chile Rise (CTJ), erodes the continental wedge due to the bathymetric highs associated to the spreading center and the roughness of the young oceanic crust around this feature (Bangs and Cande, 1997; Bourgois et al., 2000; Maksymowicz et al, 2012).

According to previous works, the principal parameters that control the first order tectonic segmentation of the Chilean continental wedge are the abrupt change of convergence velocity at the CTJ and the variation in the sediment trench fill (Fig. 1). In particular, the starved trench observed in the northern segment results from the arid climate and from the subduction of JFR that blocked the northward redistribution of sediments through the trench axial channel (Thornburg and Kulm, 1987; Völker et al., 2013). This segmentation shows the big impact of the subducted oceanic features on the tectonics of the continental wedge at a regional scale, and suggests that smaller oceanic features and/or continental structures can determine a more local variability of the tectonics of the continental wedge.

3. Method and data

3.1. Non-Cohesive Critical Coulomb Wedge modeling

Despite the complexity of the deformation style, geometry, and rheology of the observed continental wedges, it is possible to perform a first order analytical analysis of the relation between the stress field, the shape of the wedge and its internal fragile deformation using the Non-Cohesive Coulomb Wedge Theory (NCCW, Davis et al., 1983; Dahlen, 1984; Dahlen et al., 1984). This model approximates the geometry of the wedge as a triangle defined by constant angles of surface slope α and subduction angle β (see Fig. 2a). Briefly, for a homogeneous wedge (where water density ρ_w, the internal density ρ_s, the internal Hubbert–Rubey fluid pressure ratio λ, the internal friction coefficient μ, and the effective basal friction coefficient μ_b^*, remain constant), the angles α and β are related by:

$$\alpha + \beta = \Psi_b - \Psi_0 \tag{1}$$

where Ψ_0 and Ψ_b are the angles extended from the direction of the principal stress (σ_1) to the slope and to base respectively (see Fig. 2a). These angles are defined by:

$$\Psi_0 = \frac{1}{2}\arcsin\left(\frac{\sin\alpha^*}{\sin\phi}\right) - \frac{1}{2}\alpha^* \tag{2.1}$$

$$\alpha^* = \arctan\left[\left(\frac{1-\rho_w/\rho_s}{1-\lambda}\right)\tan\alpha\right] \tag{2.2}$$

$$\mu = \tan(\phi) \tag{2.3}$$

and

$$\Psi_b = \frac{1}{2}\arcsin\left(\frac{\sin\phi_b^*}{\sin\phi}\right) - \frac{1}{2}\phi_b^* \tag{3.1}$$

$$\mu_b^* = \tan\phi_b^* \tag{3.2}$$

The effective basal friction coefficient (μ_b^*) determines the Mohr–Coulomb failure criterion at the base of the wedge (interplate contact), considering the effects of the fluid pressure. This parameter decreases with an increment of the basal fluid pressure. The Hubbert–Rubey fluid pressure ratio (λ) is the ratio between the fluid pressure and the lithostatic pressure at the interior of the wedge (both pressures are referenced to the pressure at the top of the wedge), this parameter is equal to zero for a dry wedge, ρ_w/ρ_s for the hydrostatic case, and it increases in the presence of overpressure.

Using the expressions mentioned above, it is possible to build a rupture envelope (red line in Fig. 2b) formed by all wedges (i.e. all α, β pairs) that are critically rupturing (in the sense of the Mohr–Coulomb rupture criterion) with the same parameters ρ_s, λ, μ, and μ_b^*. As the internal friction coefficient μ and the direction of σ_1 are known, the conjugated internal rupture directions can be calculated for each point of the envelope. In particular, the branches of the envelope highlighted in black in Fig. 2b correspond to wedges characterized by thrust faulting and normal faulting respectively.

This analytical solution is considering a non-cohesive rupture criterion, which can be satisfied well enough in the case of wedges composed by poorly compacted sedimentary material and/or fractured rocks. It is important to note that the NCCW is a static self-similar model, which means that it is unable to describe the continuous time variation of the stress–strain field or to make prediction about a specific fault, but provides an approximate characterization of the deformation style of the continental wedge resulting from a stable forming process. In other words, it is considered that the NCCW model is useful to the study of the long-term-regional tectonics, but not for the local-short-term complexities of the deformation process.

In order to perform a quantitative interpretation of continental wedge geometry observed in the Chilean margin, I implemented a simple forward modeling to compare the rupture envelopes obtained for a set of NCCW parameters with the observed $\alpha\beta$ pairs. By using that routine, Fig. 3 shows examples of the effects of the parameter changes on the rupture envelope.

As can be observed in Fig. 3a, for constant values of λ, μ and μ_b^*, the effect of the density variation on the resulting resistance envelope is small. The accretionary branch of the envelope is very similar in a broad range of densities, and the slope angle of the erosive branch varies less than 0.5° for typical densities of the continental wedge. Therefore, I considered a constant average value of $\rho_s = 2.5$ g/cc for the entire Chilean margin. A similar effect is obtained if λ, ρ_s and μ_b^* remain constant and the internal friction coefficient μ varies in the rage of 0.470 to 0.5085 that according to Barton and Choubey (1977) represent sandstone and granite rocks respectively (see Fig. 3b). Therefore the value of 0.5085 is preferred to model the Chilean continental wedge, considering that it is formed mainly by igneous rocks and well compacted sediments

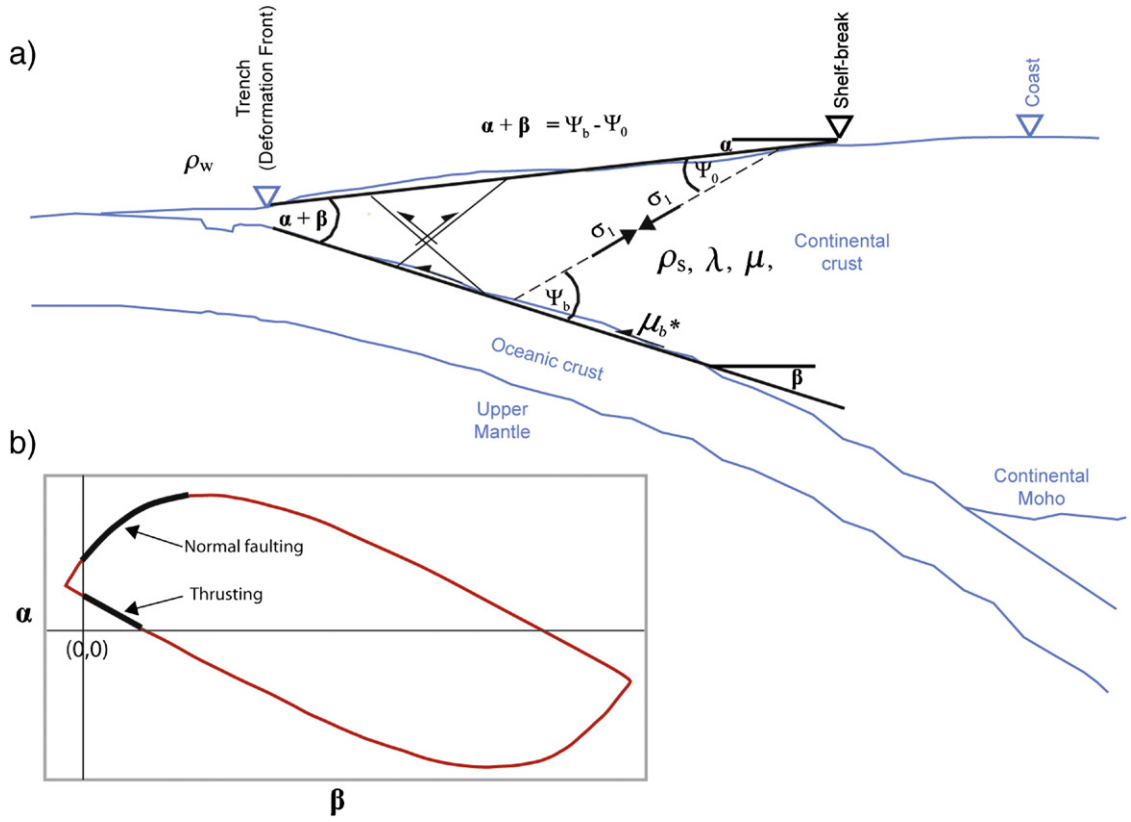

Fig. 2. Main aspects of the Non-Cohesive Critical Coulomb Wedge theory. a) Relation between the wedge geometry (α, β angles) and the direction of principal internal stresses (σ_1,σ_3). ρ_w is the water density, ρ_s is the density of the wedge, λ is the Hubbert–Rubey fluid pressure ratio, μ is the internal friction coefficient of the wedge, and μ_b* is the effective basal friction of the wedge. b) Rupture envelope of the Non-Cohesive Critical Coulomb Wedge theory in a αβ plot. The black lines are the sectors of the rupture envelope where thrusting faults and normal faulting are observed.

(see Maksymowicz et al., 2012; Moscoso et al., 2011; and Sallares and Ranero, 2005, for different latitudes).

Fig. 3c shows the variation of resistant envelope in the function of the Hubbert–Rubey fluid pressure ratio. An increase of λ determines a decrease of the slope angle α for a specific value of the subduction angle β. Similarly, an increase of the μ_b*, keeping constant the other parameters (Fig. 3d), results in a decrease of the slope angle α for a specific value of the subduction angle β.

The variation of the fluid pressure ratio (λ) and μ_b* has a large effect on the rupture envelopes (Fig. 3c and d) and there is a tradeoff between them. However, it is important to note that the variation of these parameters can have a similar tectonic interpretation since μ_b* decreases when the fluid pressure increases at the base of the wedge, and λ increases when the fluid pressure increases within the wedge. Hence if the tectonics of the margin determines a general fracturing both at the base and within the wedge (in erosive margins, for instance), μ_b* and λ can change jointly to reflect such particular tectonic condition.

In order to compare tectonic states along the Chilean margin I modeled the observed αβ data, considering a constant value of λ to derive values of μ_b* as a function of the latitude. For the accretionary parts of the Chilean margin, I considered a value of $\lambda = 0.67$, because it was measured directly in the Taiwan margin and in the Guatemala margin (Davis et al., 1983). This value is also close to the value modeled for Japan ($\lambda = 0.7$) by Cubas et al. (2013a), and is near the average value of the interval ($\sim 0.4 < \lambda < \sim 0.9$) analyzed for the different margins worldwide (see, for instance, Wang and Hu (2006) and Cubas et al., (2013b). It is possible to perform this analysis for every observed αβ pairs, but I prefer to find envelopes representative of broad segments of the margin. In fact, probably the physical parameters (like basal friction) are similar at regional scale, and the local variations of α are associated to submarine canyons and the 3-D local complexities of the deformation process cannot be modeled with the NCCW theory.

As was discussed before, the selection between the different branches of the NCCW envelope is equivalent to impose a general structural style for the wedge. In the case of the Chilean margin, the structural styles are broadly documented by numerous authors (see Section 2), then I used the corresponding lower branch of the fracture NCCW envelope to model the trust deformation of the accretionary portion of the margin, and the upper branch for the erosive portion of the margin characterized by normal faulting. I also have selected individual points of the envelope to calculate the associated principal fracture directions.

3.2. Determination of the continental slope angle (α)

In order to characterize the Chilean continental wedge using the NCCW theory, I first determined the slope angle α along the entire Chilean margin (blue line in Fig. 4a). I calculated this angle observing the position and elevation of the deformation front (DF) and the position and elevation of the shelf-break (SB) at every ~2 km along the margin (blue lines in Fig. 4b). The position and elevation of these points were determined in ~2100 E-W profiles extracted from an elevation grid generated by the merge of: (1) ETOPO1 bathymetry data (Amante and Eakins, 2009) of the National Oceanic and Atmospheric Administration (NOAA), (2) multi-beam high-resolution bathymetry data acquired along the continental slope and the trench of the Chilean margin from ~20°S to ~48°S (Bourgois et al., 2000; GEOMAR TIPTEQ Project: The Incoming Plate to mega-Thrust Earth-Quake, Flueh and Grevemeyer, 2005) and (3) SRTM (Shuttle Radar Topography Mission) topography (92 m × 92 m, resolution) for the onshore part (Rabus et al., 2003) . A subset of the resulting DF and SB

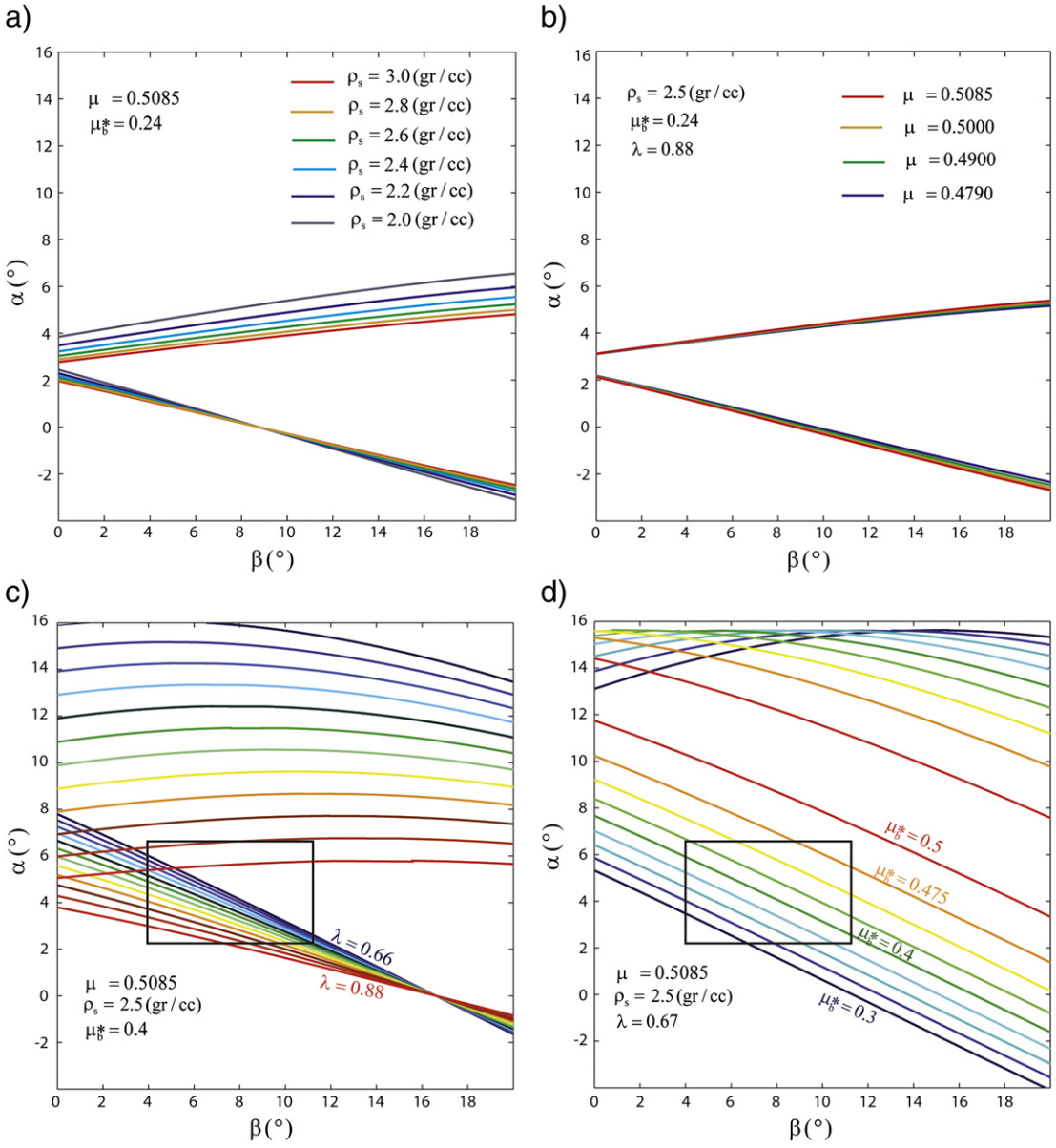

Fig. 3. Sensitivity analysis of the NCCW with internal density ρ_s, internal friction coefficient μ Hubbert–Rubey fluid pressure ratio λ and effective basal friction coefficient μ_b^*. (a) Variation of the rupture envelope for different internal densities ρ_s considering constant values of $\lambda = 0.88$, $\mu_b^* = 0.24$ and $\mu = 0.5085$. (b) Variation of the rupture envelope for different internal friction coefficients μ considering constant values of $\lambda = 0.88$, $\mu_b^* = 0.24$ and $\rho_s = 2.5$ g/cc. (c) Variation of the rupture envelope for different Hubbert–Rubey fluid pressure ratios λ considering constant values of $\mu = 0.5085$, $\mu_b^* = 0.4$ and $\rho_s = 2.5$ g/cc. Different envelopes correspond to values of λ between 0.66 and 0.88 with a sample interval of $\Delta\lambda = 0.02$. The black rectangle indicates the area where the angles α and β of the Chilean wedge are located (see Fig. 6). (d) Variation of the rupture envelope for different effective basal friction coefficients μ_b^* considering constant values of $\mu = 0.5085$, $\lambda = 0.67$ and $\rho_s = 2.5$ g/cc. Different envelopes correspond to values of μ_b^* between 0.3 and 0.5 with a sample interval of $\Delta\mu_b^* = 0.025$. The black rectangle indicates the area where the angles α and β of the Chilean wedge are located.

data was used to derive the variations of the continental wedge width in the zone between 48°S and 33°S (see Contreras-Reyes et al., 2013).

As I picked the DF and SB position in a UTM projected map, α is calculated directly from the right angle triangle formed by the E-W horizontal distance and the elevation difference between DF and SB (see the schema in Fig. 2a). This approximated α oriented E-W is representative for the slope angle α in the sectors of the Chilean margin where the trench has an approximated N-S strike, but not for the curved sectors like the Bolivian and Magallanes oroclines. Therefore, to avoid the curvature effect, I calculated a maximum α angle (maximum slope gradient, black line in Fig. 2a) by selecting, for each DF picked point, the SB picked point that results in the highest value of α. This procedure corrects for the margin curvature effect of the slope angle (see for instance the sector south of 52°S, Fig. 4a). The highest value of α is preferred here because it is theoretically equal to the values calculated in the directions perpendicular to the DF and perpendicular to the SB in zones where the DF and SB are parallel. Additionally, the maximum angle α is the version of the slope angle which is less sensitive to the local decreases of slope due to the presence of submarine canyons, and is less affected by the local strike rotations of the DF and the SB.

3.3. Determination of the subduction angle (β)

Assuming that the subduction angle of the continental wedge (β) is the angle of the slab in the shallow portion of the subduction, I generated two versions of β according to the available geophysical data (Fig. 5). The first was generated using the SLAB1 model of Hayes et al. (2012) for the latitudes north of 45°S (coverage of that model) and the values obtained by Maksymowicz (2013) and Polonia et al. (2007) for the South. According to Maksymowicz et al. (2015), the angle between 10 km and

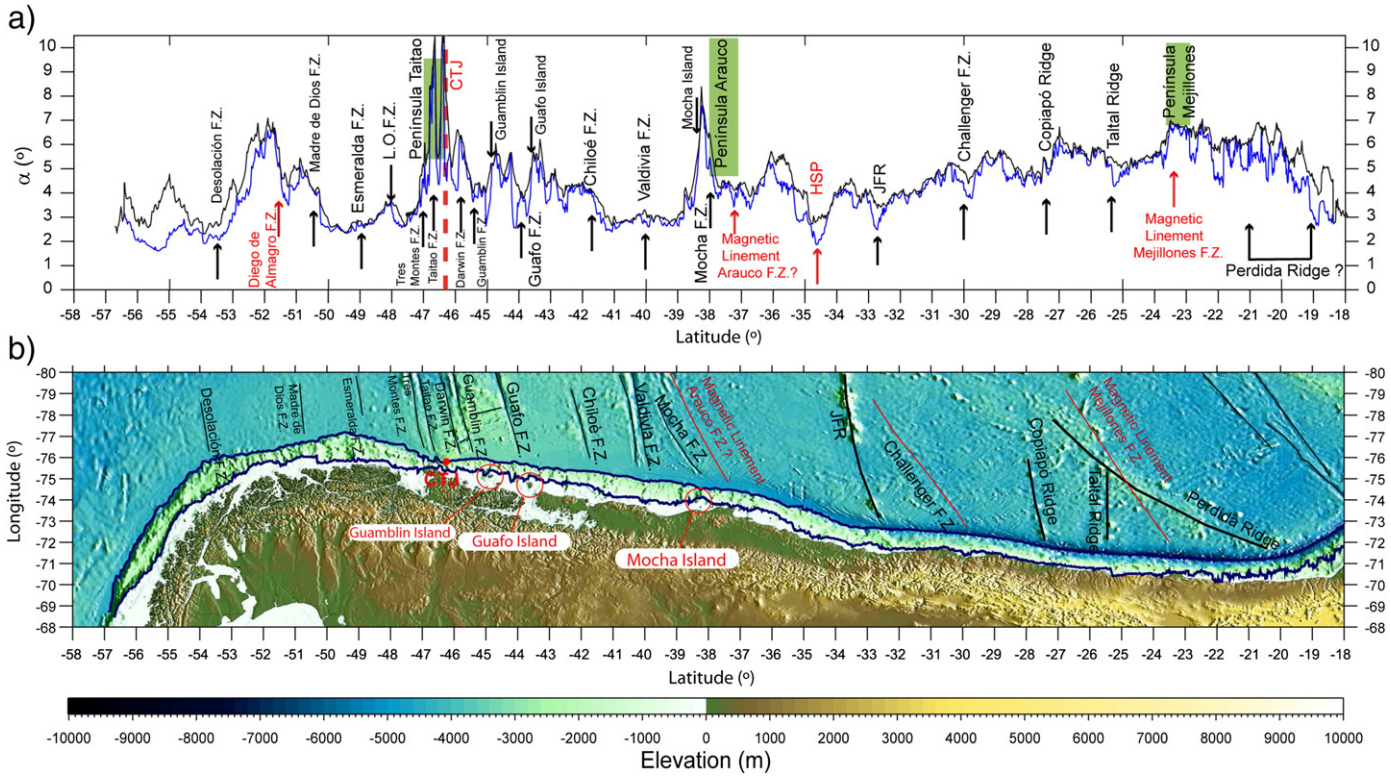

Fig. 4. Definition of the slope angle α of the Chilean continental wedge. (a) Values of the slope angle α as function of the latitude. Blue line is the W-E version and black line is the maximum value (see text for details). Arrows indicate the subduction of the oceanic features and the location of the Guamblin, Guafo and Mocha islands. The green boxes indicate the presence of the large Peninsulas and the dotted red line shows the location of the Chile Triple Junction (CTJ). (b) Elevation map of the Chilean margin. Blue lines correspond to the deformation front and shelf-break along the margin, black lines are the oceanic bathymetric features and red lines are the oceanic lineaments identified only in the magnetic signal. The red dot indicates the position of the CTJ, and the red circles show the location of the Guamblin, Guafo and Mocha islands.

20 km of slab depth is representative for the subduction angle below the continental slope in the segment between 33.5°S and 35.5°S, then the first version of β corresponds to a smooth curve that fits the angle between 10 km and 20 km of the SLAB1 model (blue line in Fig. 5). On the other hand, the previous seismic and gravimetric studies provide more accurate values of β below the continental wedge at several latitudes of the margin (Polonia et al., 2007; Maksymowicz, 2013; Scherwath et al., 2009; Contereras-Reyes et al., 2008; Moscoso et al., 2011; Maksymowicz et al., 2015; Zelt, 1999; Contereras-Reyes et al., 2014; Sallares and Ranero, 2005). Despite the high spacing between these profiles, I generated a second version of β (the "seismic version") applying a smooth interpolation between the values shown by these

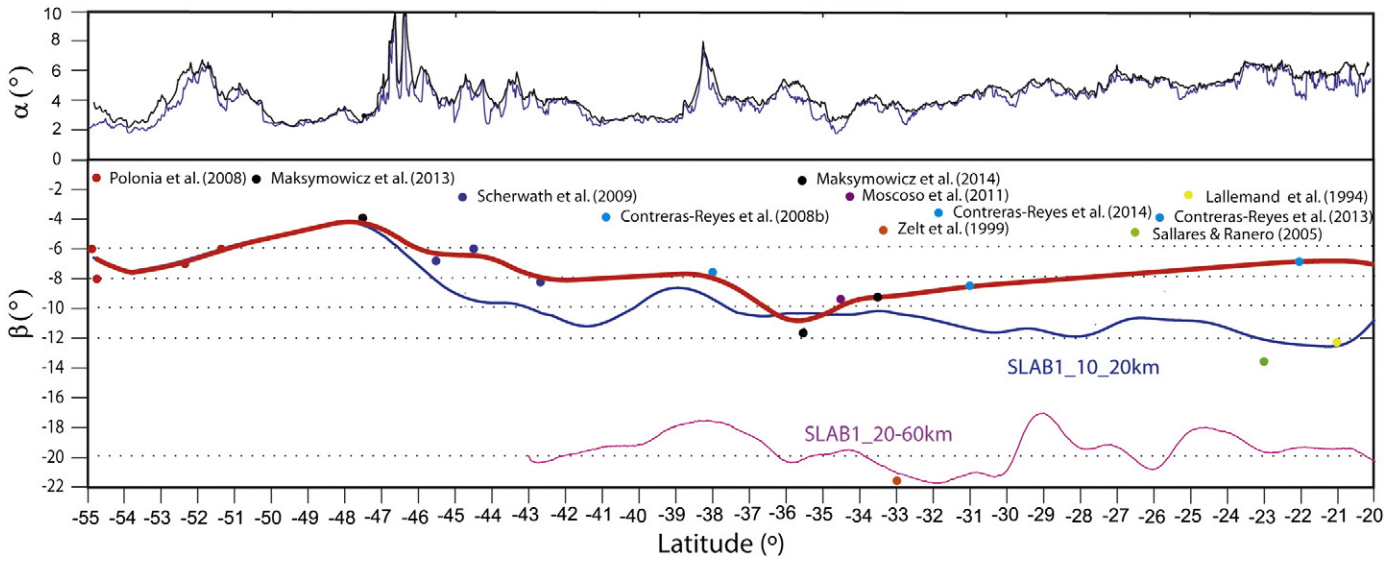

Fig. 5. Definition of the subduction angle β. Values of the subduction angle β of the continental wedge as a function of the latitude. Blue line is the version derived from the SLAB1 model from 10 to 20 km depth, magenta line is the version derived from the SLAB1 model from 20 to 60 km depth and thick red line is the preferred model derived from several seismic and gravimetric studies (see text for details), the color points indicate the value reported in each study. The upper panel shows the values of the slope angle α as function of the latitude (see Fig. 4).

authors (red line in Fig. 5). It is important to note that the high β derived from Zelt (1999) is representative for the deepest interplate contact angle (~20° at depths > 20 km), and for this reason it does not fit in the seismic version of β. Similarly the values obtained by Sallares and Ranero (2005) and Lallemand et al. (1994) were not considered because they are ~7° and ~4° higher than the ones obtained by Contereras-Reyes et al. (2012) with a well constrained wide-angle seismic tomography. Contereras-Reyes et al. (2012) found an abrupt increase of β (similar to kink geometry) at ~20 km depth, which could be characteristic of the northern Chile margin.

3.4. Mapping of oceanic features

In order to interpret the impact of the subducted structures (e.g. fracture zones, aseismic ridges) on the parameters derived from the NCCW theory, I identified them on the bathymetry map of the Chilean margin (see Fig. 4b and S1a) and also on the magnetic anomaly of the zone (see supplementary material; Fig. S1b and S1c). As is expected, much of the magnetic features can be recognized on the bathymetry except three important lineaments (red lines in Fig. 4b): (1) the fracture zone named here Mejillones FZ (subducting near ~23°S, beneath Mejillones Peninsula), which according to the age data presented by Müller et al. (2008) involves a northwestward age discontinuity < Myr; (2) the Challenger FZ (subducting near ~29.5°S) which has a remarkable magnetic expression according to its important age discontinuity (~5 Myr); and (3) the lineament named here Arauco FZ (subducting near ~37°S, below Arauco Peninsula) which seems to be a northern branch of the Mocha FZ. Finally, the fault zone named here Diego de Almagro FZ (~51.5°S) is not observed in the bathymetry neither in our magnetic map but was recognized by Cande and Leslie (1986).

4. Results

4.1. Latitudinal variation of the slope and subduction angles

Beyond the high frequency variation of the slope angle α (Figs. 4a and 5) that is explained by the presence of submarine canyons, landslides, slope basins, and local mass transfer processes, the slope angle α shows interesting characteristics at different scales.

In general, the southern half of the Chilean margin presents values of $\alpha < 5°$ and the northern half shows higher values. The limit between these two segments is located between ~33°S and ~30°S. This first order segmentation can be certainly associated with the principal tectonic change in the Chilean wedge, where the accretionary segment (south of JFR) has lower slope angles than the erosive margin to the North, as is predicted by the NCCW theory.

At smaller scale, the variation of slope angle α seems to be controlled by the presence of the oceanic and continental features at the margin. In fact, there is a remarkable correlation between the location of the fault zones, aseismic ridges and peninsulas with local anomalies of α (Fig. 4). Most of the subducted fault zones are associated to small slope angles α (Desolación FZ, Diego de Almagro FZ, Esmeralda FZ, Guamblin FZ, Valdivia FZ, Arauco FZ and Challenger FZ), three others correlate with abrupt changes of slope angles α (Madre de Dios FZ, Tres Montes FZ and Chiloé FZ), and the impact of the remaining fault zones (Taitao FZ, Darwin FZ, Mocha FZ, and Mejillones FZ) seems to be hidden by the presence of the Taitao, Arauco and Mejillones peninsulas. Similarly to the fault zones effect, the subduction of aseismic ridges also correlates with small slope angles α (JFR, Copiapo Ridge and Taltal Ridge). The opposite effect on the slope angle α is observed seaward from the large Chilean peninsulas (Mejillones Peninsula, Arauco Peninsula and Taitao Peninsula), where the slope angle α reaches the maximum values for the Chilean margin. A similar effect is observed near the Guafo, Guamblin and Mocha islands.

Fig. 6a and b shows the α vs. β graphics for the SLAB1 and the seismic versions of β. The seismic version of β decreases northward from ~10° at ~34°S to ~7° at 22°S and the SLAB1 version of β increases 2° in the same latitudes (see Fig. 5). The SLAB1 model allows us to classify the northernmost sector of the margin as a "Non-accretionary wedge" (Fig. 6a), while for the seismic version of β, the entire Chilean margin is inside or near the "Intermediate accretionary wedge" (Fig. 6b). This analysis shows the importance of a precise determination of the subduction angle β below the wedge in order to characterize the tectonics of the margin with the NCCW theory, and that the variations of the Chilean margin geometry are not clearly classified by the global domains proposed by Lallemand et al. (1994). It suggests that a more detailed classification is necessary for the Chilean and other margins after a new and more precise evaluation of the basal subduction angle β.

4.2. Effective basal friction coefficient (μ_b^*)

In this section I describe the estimations of basal friction coefficient obtained along the different segments of the Chilean margin.

4.2.1. Effective basal friction coefficient (μ_b^*) along the southern Chile margin

Fig. 7 shows the NCCW analysis south of CTJ. In Fig. 7a, I observed the geometry of continental wedge south of the Madre de Dios FZ is consistent with a μ_b^* value around 0.4 with two principal sub-segments of $\mu_b^* = 0.44$ to the south of Diego de Almagro FZ and $\mu_b^* = 0.38$ to the north of that feature (Fig. 7a). The rupture directions and the geometry of the continental wedge for the αβ point are indicated with black triangles in the left panel. The rupture directions are represented by a "beach ball" (Fig. 7a, right), inspired on the focal mechanism for earthquakes, where the rupture planes are not perpendicular because they are the conjugated rupture directions according to the internal friction and fluid pressure. The predicted deformation style is described by 40° to 45° west dipping reverse faults and 17° to 20° east dipping reverse faults (Fig. 7a, right).

The segment immediately south of CTJ is characterized by a low value $\mu_b^* = 0.275$ (Fig. 7b). It is interesting to note that long segments are explained by a unique rupture envelope, which supports the application of this simple model to derive regional physical information from the wedge geometry. The deformation style is described by 37° west dipping reverse faults and 28° east dipping reverse faults (Fig. 7b, right).

4.2.2. Effective basal friction coefficient (μ_b^*) along the central Chilean margin

The NCCW analysis divides the area between the CTJ to the JFR subduction (~33°S) into two segments, the southern segment from 46°S to 39°S with subduction angles β ranging from ~6° to ~8° (Fig. 8a), and the northern segment from 37.5°S to 33°S with subduction angles β from ~8° to ~11° (Fig. 8b). Applying a constant fluid pressure ratio, $\lambda = 0.67$, the geometry of the continental wedge south of the Arauco Peninsula is explained by $\mu_b^* > \sim 0.35$. South of Chiloé FZ (~41.5°S) the rapid variations of the slope angle α correlate with the presence of numerous fracture zones and isolated islands in the shelf (see Fig. 8a), which generates a complex αβ curve. Then, I fit an average regional curve ($\mu_b^* = 0.4$) representative mostly for the northern portion of this subsegment. On the other hand, from the Chiloé FZ to the Arauco Peninsula, the value of $\mu_b^* = 0.35$ can explain all the observations. The rupture direction analysis indicates that the predicted deformation style is described by 37° to 40° west dipping reverse faults and 20° to 25° east dipping reverse faults (Fig. 8a, right).

Between the Arauco Peninsula and the Juan Fernández Ridge, the geometry of the continental wedge between the Arauco Peninsula and the JFR is consistent with μ_b^* in the range of ~0.385 to ~0.465 (Fig. 8b). In this case, a south to north sequence of sub-segments is identified with values of $\mu_b^* = 0.415$, $\mu_b^* = 0.465$, $\mu_b^* = 0.385$ and $\mu_b^* = 0.415$,

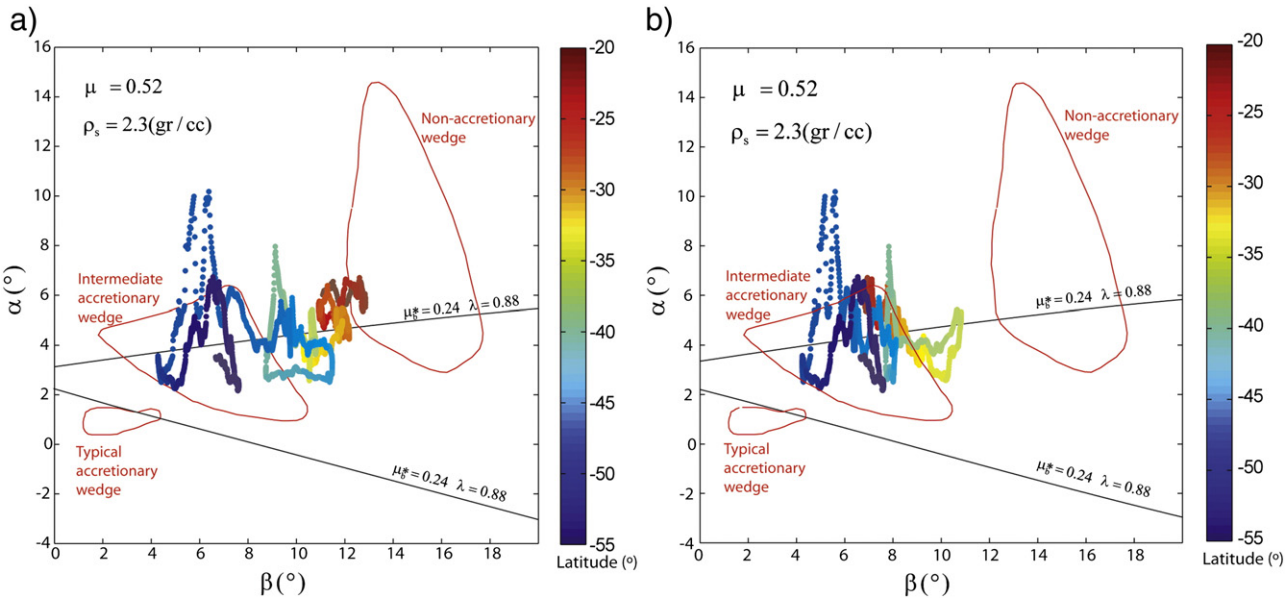

Fig. 6. Slope angle α vs. basal angle β for the entire Chilean margin, latitudes are color coded. Solid black lines correspond to the NCCW rupture envelope for the parameters λ, μ_b^*, μ and ρ_s analyzed by Lallemand et al. (1994) and the red lines are the classification of the convergent margins of the same author. (a) Considered the SLAB1 model. (b) Considered the preferred seismic model of the subduction.

where the low friction segment between ~35°S and ~34°S correlates with the high slip patch of the Maule 2010 earthquake (Moreno et al., 2012). The predicted deformation style is characterized by 37° to 45° west dipping reverse faults and 20° to 28° east dipping reverse faults (Fig. 8b, right).

4.2.3. Effective basal friction coefficient (μ_b^*) along the northern Chilean margin

North of JFR subduction (~33°S) it is necessary to consider a remarkable decrease of the μ_b^* values jointly with an increase of the λ value. If a value of $\lambda = 0.8$ is set, the geometry of the continental wedge for northern Chile is explained by a μ_b^* ranging from 0.05 to 0.19 (Fig. 9a). Regionally, a systematic northward increase of μ_b^* suggests a sub-segmentation of the northern Chilean margin: (1) from the JFR to ~29.5°S the wedge geometry can define an increment of μ_b^* from 0.005 to 0.11, and (2) to the North, three sub-segments with values of about 0.11, 0.14 and 0.19. However, the definition and interpretation of these sub-segments are only approximate due to the rapid slope angle variations. The predicted deformation style is characterized by 35° to 45° west dipping normal faults and 75° to 80° east dipping normal faults (Fig. 9a, right).

Despite the tradeoff between μ_b^* and λ, the change of the parameters between the accretionary and erosive segment of the margin is also found. If for instance, a greater value $\lambda = 0.87$ is considered for the northernmost portion of the margin, the basal friction coefficient increases from 0.19 to 0.4 similar to the ones observed in the accretionary zone (dashed lines in Fig. 9a). However, for the initial (lower) values of μ_b^*, I find that the deformation style predicted by NCCW corresponds to a set of 35° west dipping normal fault and 80° east dipping normal fault, while for the higher value of μ_b^* I find a 75° west dipping reverse fault and a 15° west dipping normal fault. According to the reflection seismic profile, located at ~23°S, the first parameter set ($\mu_b^* = 0.14$, $\lambda = 0.8$) that produces high angle normal faults is quite precise to describe the deformation style of the continental wedge at the latitude of Mejillones Peninsula, and also, it is representative for the general deformation style north of the 33°S (see Ranero et al., 2006; Contreras-Reyes et al., 2014; and Fig. 9b).

5. Interpretation and discussion

In general terms, the latitudinal analysis of the margin slope angle α and the subduction angle β and the results of the NCCW model for the continental wedge suggest the existence of a first and a second order segmentation in the tectonic state of the Chilean margin.

The first order segmentation is related to the transition between the accretionary and erosive margin (~33°S, JFR subduction) that corresponds to a general increase in the slope angle α of the erosive margin relative to the southern accretionary segment, which is predicted by the NCCW theory (Dahlen, 1984). This limit also corresponds to an important variation of values of μ_b^* and at the same latitudes where μ_b^* decreases from values around 0.4 to values of about 0.1 and λ increases from 0.67 to 0.8. Despite the tradeoff between the parameters μ_b^* and λ, a decrease of μ_b^* and/or an increase of λ are necessary to explain the geometry of the continental wedge, and the deformation style observed in the seismic reflection profile (see an example in Fig. 9b). The sense of the variations observed in the parameters μ_b^* and λ can be interpreted by an increase of the fracturing that favors the increment of the fluid pressure, both at the base and inside the wedge. This can be explained by the impact of a rough slab beneath the base of the wedge and the pervasive failure of gravitational collapse typical of the erosive margins. The result suggests that the tectonic erosion could be a process characterized by low basal effective friction coefficients which is relevant for the geodynamic evolution and seismotectonic interpretations of subduction zones. It is interesting to note that the zone located south of the CTJ, where the low convergence rate favors a large accretionary prism, has sectors with slope angles α similar to that observed in sectors of the central accretionary zone (compare for instance the 50°S–47°S segment with the 41°S–30°S segment). This suggests that the size of the accretionary prism could not be a key parameter to explain the observed slope angles α.

The second order tectonic segmentation of the Chilean continental wedge can be described as a sequence of segments with different values of α, μ_b^* and/or λ, limited by the presence of fracture zones, bathymetric highs, and seaward continental prolongations, which locally modify the geometry of the continental wedge.

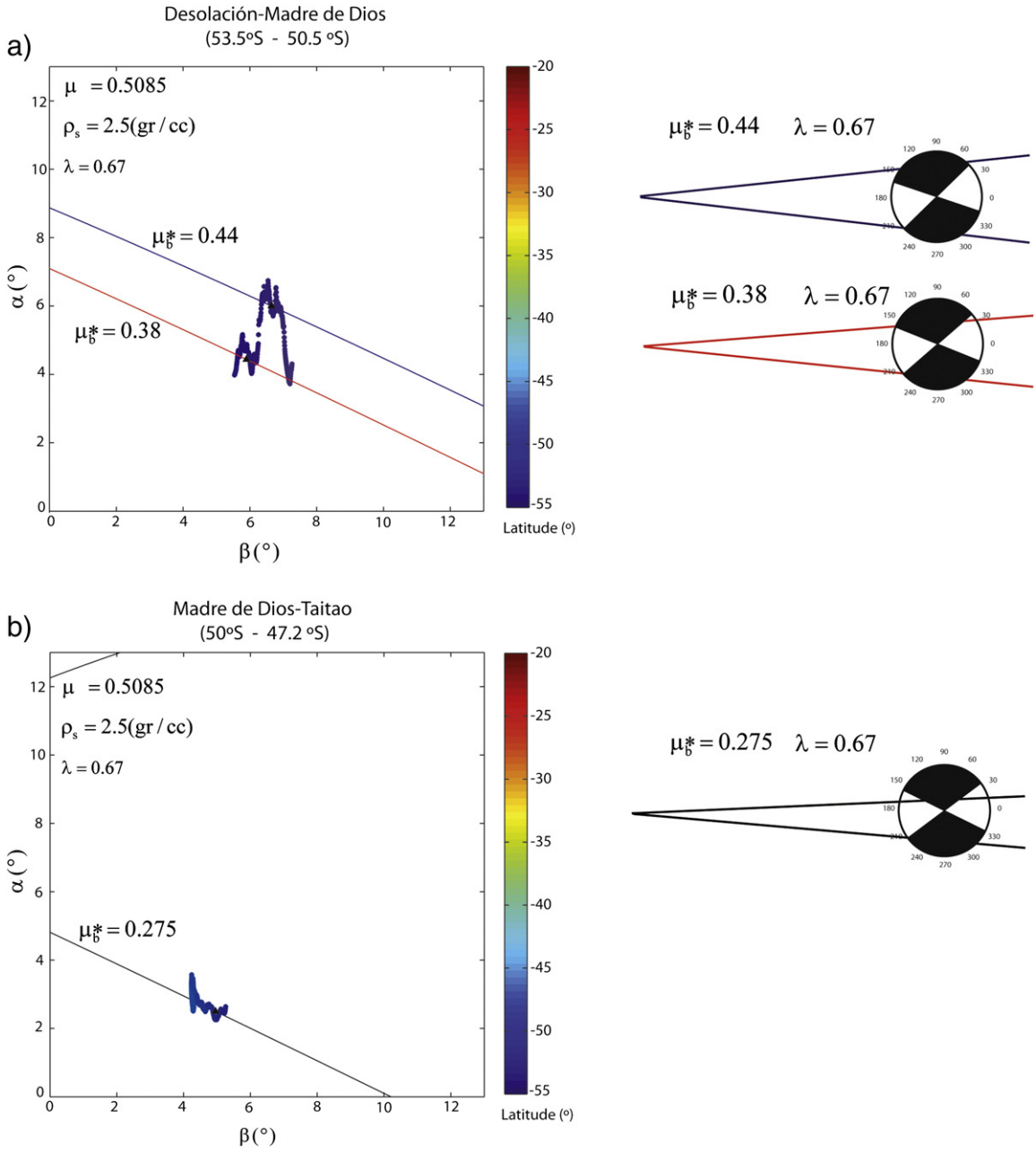

Fig. 7. NCCW analysis for the southern Chile margin. (a) The dots are the αβ data from 53.5°S to 50.5°S (the latitudes are shown in the color bar). Solid lines correspond to the NCCW rupture envelopes for different values of μ_b^* considering constant values of $\lambda = 0.67$, $\rho_s = 2.5$ g/cc and $\mu = 0.5085$ as in Fig. 3d. At the right of the αβ diagram, for each black triangle, a schema of the predicted continental wedge geometry and the principal rupture direction is shown. (b) Same analysis as (a) but with the αβ data from 50.5°S to 47.2°S.

According to the NCCW theory and sand analog experiments (Dahlen et al., 1984; Guthscher et al., 1996), a decrease of the slope angle α is explained by a decrease of the effective basal friction μ_b^*, which in turn, descends with the increase of pore fluid pressure at the base. Then if the more hydrated oceanic lithosphere of the fault zones releases fluids to the interplate contact, the slope angle α should decrease in the fault zone subduction areas, such as is observed along the Chilean margin (Fig. 4). The subduction of a seamount (or a seamounts chain) has a short-term local impact on the continental wedge tectonics, fracturing the continental basements and modifying the slope angle α during the subduction process. Seismic studies and analogous experiments (Dominguez et al., 2000; Kodaira et al., 2000; Park et al., 1999) showed that initially, the frontal slope angle increases during the seamount subduction, but afterwards the continental wedge experiences subsidence and the frontal slope angle α decreases. This short-term process also generates pervasive fracturing in the continental wedge, which can favor the fluid infiltration of the basement and the interplate contact, incrementing the fluid pressure and decreasing the effective basal friction μ_b^* and the slope angle α. In fact, as is discussed by Maksymowicz et al. (2015), the zone of high slip patch of the Maule 2010 Mw8.8 earthquake that corresponds to a minimum in α angle (HSP anomaly in Fig. 4a), also corresponds to a segment with low effective basal friction coefficient μ_b^*, and according to gravity models, with the presence of a possible subducted seamount Maksymowicz et al. (2015). The impact of the seamount subduction on the margin probably is accentuated in the case of the successive

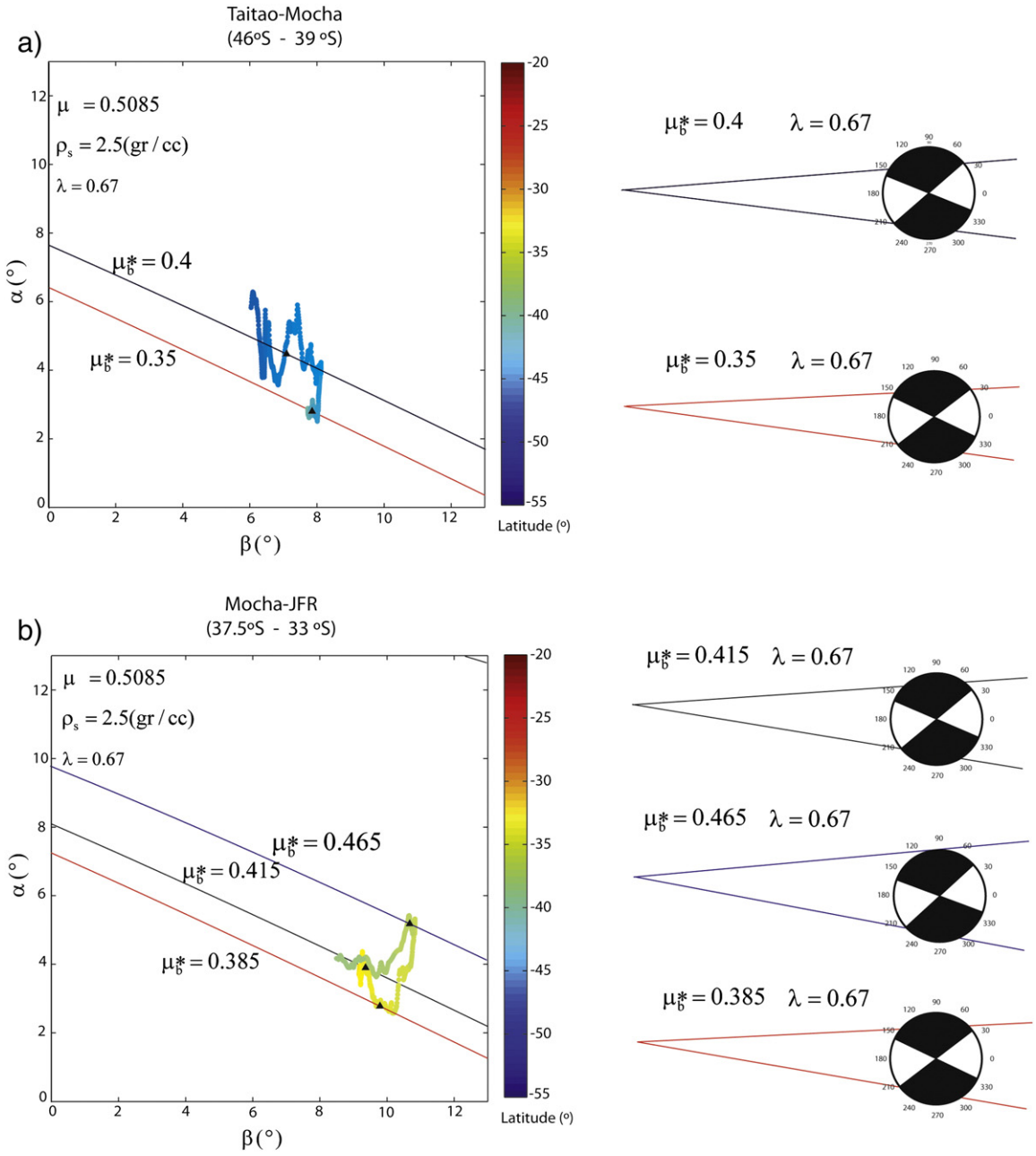

Fig. 8. NCCW analysis for the central Chile margin. (a) The dots are the αβ data from 46°S to 39°S (the latitudes are shown in the color bar). Solid lines correspond to the NCCW rupture envelopes for different values of μ_b^* considering constant values of $\lambda = 0.67$, $\rho_s = 2.5$ g/cc and $\mu = 0.5085$ as in Fig. 3d. At the right of the αβ diagram, for each black triangle, a schema of the predicted continental wedge geometry and the principal rupture direction is shown. (b) Same analysis of (a) but with the αβ data from 37.5°S to ~33°S.

seamounts subduction that forms the aseismic ridges: JFR, Copiapo Ridge and Taltal Ridge, which can explain the important local decreases observed in the analysis of the slope angle α. In contrast, I do not observe a clear effect associated with the subduction of the wide and smooth Perdida Ridge. The long wavelength of this feature can affect a broad segment of the margin but the high frequency variation of the slope angle α in the zone may hinder its effect on the continental wedge shape.

The Taitao Peninsula area corresponds to an erosive segment of the margin generated by the subduction of the rough bathymetry of the Chile Rise spreading center (Bangs and Cande, 1997; Bourgois et al., 2000; Maksymowicz et al, 2012), and then it exhibits a high slope angle α typical for tectonic erosion. On the other hand, in the accretionary segments, the increase of the slope angle α in the zones of Peninsulas and islands can be related to the presence of local anomalies of rigid basement. According to the numerical models presented by Ruh et al. (2013), in front of a local seaward extension of the rigid backstop the slope angle is high compared to the adjacent zones, which suggests that the presence of bathymetric highs on the continental wedge (Guafo, Guamblin, Mocha islands and Arauco Peninsula) can be related to anomalous rigid basement below the marine forearc basin. Such a correlation of the location of the basement high with an anomalous rigid basement/backstop has been found in other convergent margins before, e.g. Krabbenhoeft et al. (2010) for the Indonesian margin. An alternative and probably complementary explanation is the increase of the basal friction coefficient μ_b^*, which can generate high slope angles

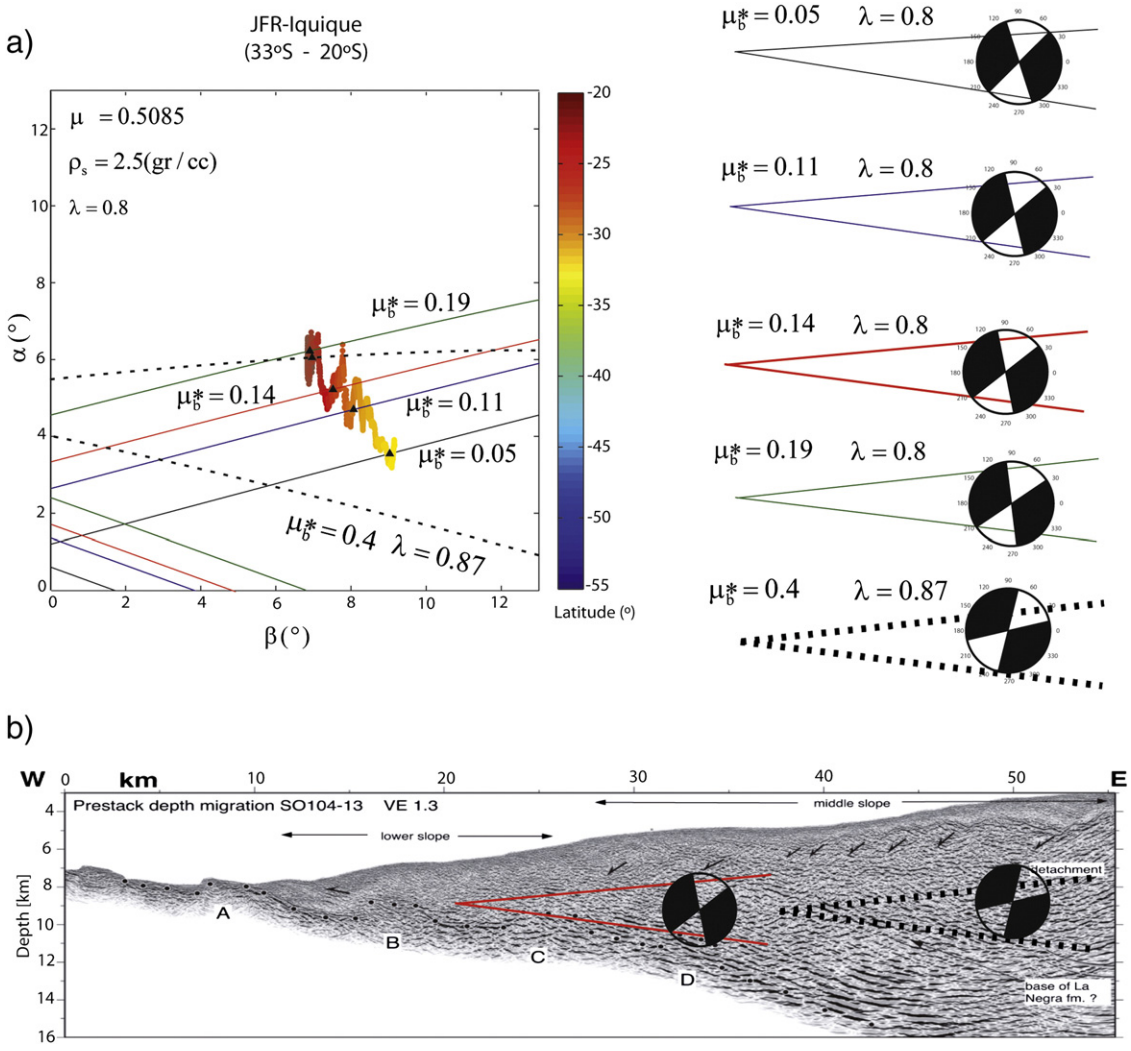

Fig. 9. NCCW analysis for the northern Chile margin. (a) The dots are the αβ data of the northern Chilean margin from ~33°S to 20°S (the latitudes are shown in the color bar). Solid lines correspond to the NCCW rupture envelopes for different μ_b^* values considering constant values of $\lambda = 0.8$, $\rho_s = 2.5$ g/cc and $\mu = 0.5085$. Dashed line is the NCCW rupture envelope for $\mu_b^* = 0.4$ and constant values of $\lambda = 0.87$, $\rho_s = 2.5$ g/cc and $\mu = 0.5085$. At the right of the αβ diagram, for each black triangle, a schema of the predicted continental wedge geometry and the principal rupture direction is shown. (b) Comparison between two predicted geometries for the continental wedge and the rupture directions with a reflection seismic profile at the latitude of ~23°S (modified from Ranero et al. (2006)).

α and low angle inverse faulting that favors the formation of duplexes at the base of the wedge and the uplift of the basement below the forearc basins Gutscher et al. (1996).

The segment of the margin where Mejillones Peninsula is located can also be interpreted as a zone with a high basal friction coefficient μ_b^*. According to Casquet et al. (2014), the metamorphic and igneous basement observed at the western limit of the Mejillones Peninsula corresponds to a Late Triassic block interpreted as a transcurrent terrane that reached its actual position at the Jurassic–Early Cretaceous time. It suggests that the rheology of this feature could be different than the surrounding basement at the zone, which can be related to the observed morphologic anomaly of the continental wedge at this latitude.

Fig. 10 shows the proposed second order tectonic segmentation of the Chilean continental wedge. The names are assigned according to the main features observed at the corresponding latitudes. As it is observed, the slope angle correlates with the estimation of μ_b^*, that is explained by the smooth curve of β values, but it could change with future models of the initial subduction angles. The sector of the αβ graphic where the geometry of Chilean wedge is plotted (black rectangle in Fig. 3c and d) shows μ_b^* variations of about 0.04 per each α degree (i.e. $\partial\mu_b^*/\partial\alpha \sim 0.04$), considering the lower branch of the NCCW envelope, and $\partial\mu_b^*/\partial\alpha \sim 0.035$ for the erosive portion of the margin (see Fig. 9a). Then, if the high value (0.04) is considered, and observing that the maximum variability of α is about ±0.5° for a specific segment of the margin (see Figs. 7 to 9a), it is possible to estimate an error of ±0.02 for the calculated values of μ_b^*. Fig. 10 shows that even considering the estimated error, the changes of μ_b^* values along the Chilean are clear, which supports the interpretation of a second order tectonic segmentation of the Chilean continental wedge.

Clearly, it is possible to refine this segmentation with shorter subsegments, but in that case the local characterization of oceanic and continental 3-D structures becomes imperative, and the simple NCCW model can be inadequate to explain the geometry of the wedge at local scale. In my view, the parameters derived from the NCCW model are representative for the geological time-scale (long-term) cumulative deformation process, and it does not have a resolution to predict the direction of a specific fault, the episodic effect of a seamount subduction, or the coseismic μ_b^* variation during the rupture of the interplate earthquakes. However, the second order segmentation presented here, is valuable to identify specific zones where the geodynamics of the Chilean margin seems to be different. This segmentation will be tested by future studies to characterize the oceanic crust, the basement of the continental wedge and the relationship between the onshore and offshore tectonics of the Chilean forearc.

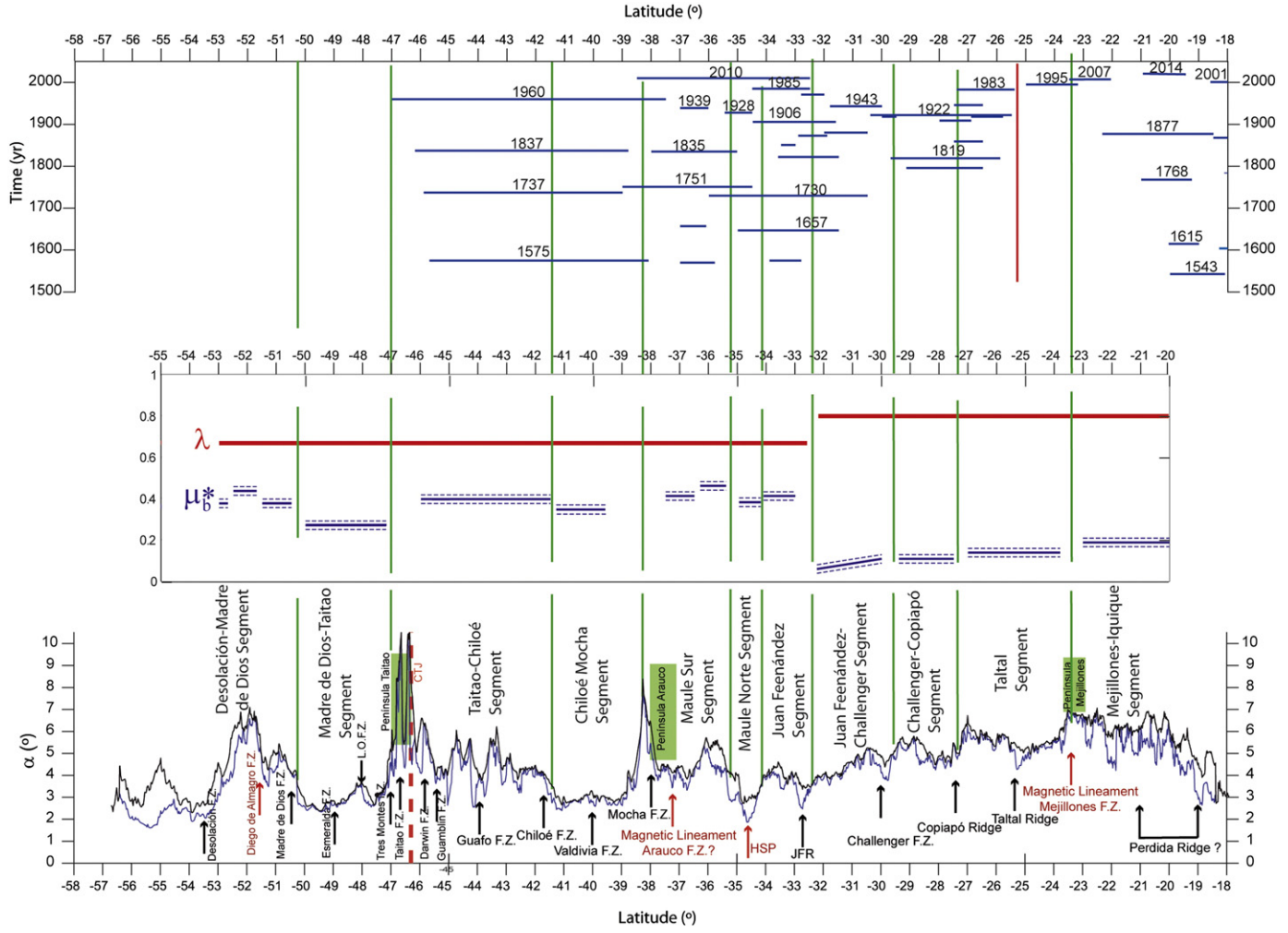

Fig. 10. Definition of the second order tectonic segmentation of the Chilean continental wedge. The lower panel shows the values of the slope angle αas a function of the latitude (see Fig. 4 for details). The suggested names for the tectonic segments of the continental wedge are shown between the green lines. The central panel shows the parameters derived from the NCCW model. Blue lines are the values of effective basal friction coefficient μ_b^* (Figs. 7 to 9), dotted blue lines correspond to the maximum error estimated for μ_b^* (see Section 5 for details), red lines are the values of the Hubbert–Rubey fluid pressure ratio λ considered, and green lines correspond to the limits between tectonic segments of the continental wedge. The upper panel shows the correlation between tectonic segmentation of the Chilean continental wedge and the rupture zones of large Chilean earthquakes. The blue lines correspond to the historical and instrumentally registered large earthquakes in Chile according to Comte and Pardo (1991), Beck et al. (1998), Cisternas et al.(2005), Ruegg et al. (2009), Bilek (2010) and the reports of the Chilean National Seismological Center [www.sismologia.cl]. Numbers are the years of the principal events, green lines are the limits between tectonic segments of the continental wedge, and the red line indicates a seismogenic limit correlated to the position of Taltal Ridge.

Maksymowicz et al. (2015) studied the spatial correlation between the high slip patch of the Maule 2010 Mw8.8 earthquake and the decrease of the slope angle α, μ_b^* and weight of the continental wedge (HSP in Figs. 4 and 10). That correlation suggests that the long-term tectonic evolution and the rheology of the continental wedge can be related to the short-term process of coseismic rupture by controlling, in part, the stress state of the margin below the slope. According to the present work, the high slip patch of the Valdivia 1960 Mw9.6 earthquake (Barrientos and Ward., 1990; Moreno et al., 2009) correlates almost exactly with the Chiloé–Mocha segment defined here, which corresponds to a zone of low μ_b^* (Fig. 10). This result and the correlation between low free-air gravity data and the high slip patch of the Valdivia earthquake (showed by Wells et al., 2003), suggest a similar behavior to that observed for the Maule earthquake.

The upper panel in Fig. 10 shows the limits of the proposed segmentation over the rupture extensions of the historic and instrumentally registered earthquakes (Comte and Pardo, 1991; Beck et al., 1998; Cisternas et al., 2005; Ruegg et al., 2009; Bilek, 2010; and the catalog of Chilean National Seismological Center, CSN). As was discussed by Contreras-Reyes and Carrizo (2011), the high oceanic features (aseismic ridges, oceanic fracture zones and the Chile Rise spreading center) coincide with the limits of the large earthquakes, and then the proposed long-term segmentation shows almost the same correlation. Differences can be found in the Maule–Norte segment (HSP) that seems to be an approximated limit between the ruptures south of the Maule Region (1835–1751) north of the Maule region (1730, 1906, 1985). Nevertheless, it is not a barrier for the rupture of Maule 2010 earthquake. Another difference is observed at the Taltal Ridge where the limit between the 1983 and 1985 earthquakes is well defined, but where there is not a clear variation of slope angle α between the south and north of the ridge. The observed correlation between the proposed segmentation and the earthquake distribution suggests that segments with different long-term parameters μ_b^*, λ can have different short-term parameters μ_b^*, λ, that can affect the stress state during the seismic cycle and the complex sequence of coseismic activation, but also the variation of these parameters can be related to the slip inhomogeneities during large coseismic ruptures.

Contreras-Reyes and Carrizo (2011) proposed that the high oceanic features locally increase the interplate coupling according to the buoyancy of these structures and I observed in general local decrease of the

slope angle at the same latitudes, interpreted as a decrease of the basal effective friction coefficient or as an effect of gravitational collapse after the subduction of the oceanic features. In the case of aseismic ridges (JFR, Copiapó Ridge and Taltal Ridge), the relation between the increase of coupling and the collapse of the continental wedge seems to be direct. On the other hand, some fracture zones in different tectonic settings (e.g. Challenger FZ and Diego de Almagro FZ) do not have a big bathymetric expression but produce a remarkable decrease in the continental wedge slope angle α, which suggests that the fluids provided by the fracture zones play a key role in the continental wedge geometry and may be consequently in the coseismic rupture processes. Finally, for the case of fracture zones that are subducting beneath the Arauco and Mejillones peninsulas (i.e., Mocha FZ and Mejillones FZ) it is important also to evaluate the effect of an anomalous continental basement to understand the generation of these important seismic barriers.

6. Conclusions

(1) The size of the frontal accretionary prism does not correlate with the slope angle α, which is controlled by the friction and fluid pressure of the entire continental wedge including the continental basement and/or paleo-accretionary prism.
(2) My version of the subduction angle β (based on seismic and gravimetrical information) classified the entire Chilean margin (including erosive and accretionary segments) near the "Intermediate accretionary wedge" definition of Lallemand et al. (1994). It reveals that a more detailed classification is necessary for the Chilean and other margins, after a new and more precise evaluation of the basal subduction angles β.
(3) The Chilean margin presents a first order segmentation according to the slope angle α and the parameters derived from NCCW theory. A general increase of the slope angle α, a decrease of the effective basal friction coefficient μ_b^* and an increase of the fluid pressure inside the continental wedge are observed at the erosive segment of the margin (north of ~33°S). This important change is interpreted as a result of a more pervasive fracturing due to tectonic erosion both at the base and within the continental wedge.
(4) The NCCW model of the Chilean margin leads to a second order tectonic segmentation of the Chilean continental wedge. These segments of the Chilean margin with different values of μ_b^* and/or λ are limited by fault zones, bathymetric highs, and seaward continental prolongations that locally modify the geometry of the continental wedge.
(5) The second order tectonic segmentation of the Chilean margin correlates with the rupture zones of the large earthquakes and with slip patches of megathrust earthquakes, which supports the concept that segments with different long-term evolution can have different stress states during the seismic cycle, affecting the complex sequence of seismic activation and also the location of inhomogeneities during large coseismic ruptures.

Acknowledgments

Andrei Maksymowicz gratefully acknowledges a scholarship granted by the Chilean National Science Cooperation (CONICYT). This work was partially supported by the PRS (Seismic Risk Program) of the DGF-University of Chile and the projects CONICYT #USA2012-001 and FONDECYT 3150160. Finally, the author thanks the detailed comments formulated by the anonymous reviewers.

Appendix A. Supplementary data

Supplementary data to this article can be found online at http://dx.doi.org/10.1016/j.tecto.2015.08.007.

References

Amante, C., Eakins, B.W., 2009. ETOPO1 1 Arc-Minute Global Relief Model: Procedures, Data Sources and Analysis. NOAA Technical Memorandum NESDIS NGDC-24. National Geophysical Data Center, NOAA. http://dx.doi.org/10.7289/V5C8276M.
Angermann, D., Klotz, J., Reigber, C., 1999. Space-geodetic estimation of the Nazca–South America Euler vector. Earth Planet. Sci. Lett. 171 (3), 329–334.
Bangs and Cande, 1997. Episodic development of a convergent margin inferred from structures and processes along the southern Chile margin. Tectonics 16 (3), 489–503.
Barrientos, S.E., Ward, S.N., 1990. The 1960 Chile earthquake: inversion for slip distribution from surface deformation. Geophys. J. Int. 103, 589–598. http://dx.doi.org/10.1111/j.1365-246X.1990.tb05673.x.
Barton, N.R., Choubey, V., 1977. The shear strength of rock joints in theory and practice. Rock Mech. 10 (1-2), 1–54.
Beck, S., Barrientos, S., Kausel, E., Reyes, M., 1998. Source characteristics of historic earthquakes along the central Chile subduction zone. J. S. Am. Earth Sci. 11, 115–129.
Bilek, S.L., 2010. Seismicity along the South American subduction zone: review of large earthquakes, tsunamis, and subduction zone complexity. Tectonophysics 495, 1–2. http://dx.doi.org/10.1016/j.tecto.2009.02.037.
Bourgois, J., Guivel, C., Lagabrielle, Y., Calmus, T., Boulague, J., Daux, V., 2000. Glacial-interglacial trench supply variation, spreading-ridge subduction, and feedback controls on the Andean margin development at the Chile triple junction area (45–48°S). J. Geophys. Res. 105 (B4), 8355–8386.
Cande, S.C., Leslie, R.B., 1986. Late Cenozoic tectonics of the southern Chile Trench. J. Geophys. Res. 91, 471–496.
Casquet, C., Hervé, F., Pankhurst, R.J., Baldo, E., Calderón, M., Fanning, C.M., Rapela, C., Dahlquist, J., 2014. The Mejillonia suspect terrane (northern Chile): Late Triassic fast burial and metamorphism of sediments in a magmatic arc environment extending into the Early Jurassic. Gondwana Res. 25 (3), 1272–1286.
Catalog of the Chilean National Seismological Center (CSN). www.sismologia.cl.
Cisternas, M., Atwater, B.F., Torrejón, F., Sawai, Y., Machuca, G., Lagos, M., Eipert, A., Youlton, C., Salgado, I., Kamataki, T., Shishikura, M., Rajendran, C.P., Malik, J.K., Rizal, Y., Husni, M., 2005. Predecessors of the giant 1960 Chile earthquake. Nature 437, 404–407. http://dx.doi.org/10.1038/nature03943.
Clift, P., Vannucchi, P., 2004. Controls on tectonic accretion versus erosion in subduction zones: implications for the origin and recycling of the continental crust. Rev. Geophys. 42, RG2001. http://dx.doi.org/10.1029/2003RG000127.
Comte, D., Pardo, M., 1991. Reappraisal of great historical earthquakes in the northern Chile and southern Peru seismic gap. Nat. Hazards 4, 23–44. http://dx.doi.org/10.1007/BF00126557.
Contreras-Reyes, E., Carrizo, D., 2011. Control of high oceanic features and subduction channel on earthquake ruptures along the Chile–Peru subduction zone. Phys. Earth Planet. Inter. 186, 49–58. http://dx.doi.org/10.1016/j.pepi.2011.03.002.
Contreras-Reyes, E., Osses, A., 2010. Lithospheric flexure modeling seaward of the Chile trench: implications for oceanic plate weakening in the Trench Outer Rise region. Geophys. J. Int. 182 (1), 97–112. http://dx.doi.org/10.1111/j.1365-246X.2010.04629.x.
Contreras-Reyes, E., Grevemeyer, I., Flueh, E.R., Reichert, C., 2008. Upper lithospheric structure of the subduction zone offshore of southern Arauco peninsula, Chile, at ~38°S. J. Geophys. Res. 113, B07303. http://dx.doi.org/10.1029/2007JB005569.
Contreras-Reyes, E., Flueh, E.R., Grevemeyer, I., 2010. Tectonic control on sediment accretion and subduction off south central Chile: implications for coseismic rupture processes of the 1960 and 2010 megathrust earthquakes. Tectonics 29, TC6018. http://dx.doi.org/10.1029/2010TC002734.
Contreras-Reyes, E., Jara, J., Grevemeyer, I., Ruiz, S., Carrizo, D., 2012. Abrupt change in the dip of the subducting plate beneath north Chile. Nat. Geosci. 5, 342–345. http://dx.doi.org/10.1038/ngeo1447.
Contreras-Reyes, E., Jara, J., Maksymowicz, A., Weinrebe, W., 2013. Sediment loading at the southern Chilean trench and its tectonic implications. J. Geodyn. 66, 134–145. http://dx.doi.org/10.1016/j.jog.2013.02.009.
Contreras-Reyes, E., Becerra, J., Kopp, H., Reichert, C., Díaz-Naveas, J., 2014. Seismic structure of the north-central Chile convergent margin: subduction erosion of a paleomagmatic arc. Geophys. Res. Lett. 41 (5), 1523–1529. http://dx.doi.org/10.1002/2013GL058729.
Cubas, N., Avouac, J.P., Leroy, Y.M., Pons, A., 2013a. Low friction along the high slip patch of the 2011 Mw 9.0 Tohoku-Oki earthquake required from the wedge structure and extensional splay faults. Geophys. Res. Lett. 40, 4231–4237. http://dx.doi.org/10.1002/grl.50682.
Cubas, N., Avouac, J.P., Souloumiac, P., Leroy, Y.M., 2013b. Megathrust friction determined from mechanical analysis of the forearc in the Maule earthquake area. Earth Planet. Sci. Lett. (ISSN: 0012-821X) 381, 92–103. http://dx.doi.org/10.1016/j.epsl.2013.07.037.
Dahlen, F.A., 1984. Noncohesive critical Coulomb wedges: an exact solution. J. Geophys. Res. 89 (10), 125–133.
Dahlen, F.A., Suppe, J., Davis, D.M., 1984. Mechanics of fold- and thrust belts and accretionary wedges: cohesive Coulomb theory. J. Geophys. Res. 8 (9), 10,087–10,101.
Davis, D.M., Suppe, J., Dahlen, F.A., 1983. Mechanics of fold- and thrust belts and accretionary wedges. J. Geophys. Res. 88, 1153–1172.
Diaz-Naveas, J., 1999. (Dissertation zur Erlangung des Doktorgrades), Christian-Albrechts-Universitat zu Kiel (130 p).

Dominguez, S., Malavieille, J., Lallemand, S.E., 2000. Deformation of accretionary wedges in response to seamount subduction: insights from sandbox experiments. Tectonics (ISSN: 0278-7407) 19. http://dx.doi.org/10.1029/1999TC900055.

TIPTEQ SONNE Cruise SO-181, from the incoming plate to mega thrust earthquakes. In: Flueh, E.R., Grevemeyer, I. (Eds.), Geomar Rep. 102. Geomar, Kiel, Germany

Gutscher, M.A., Kukowski, N., Malavieille, J., Lallemand, S., 1996. Cyclical behavior of thrust wedges: Insights from high basal friction sandbox experiments. Geology 24 (2), 135–138.

Hayes, G.P., Wald, D.J., Johnson, R.L., 2012. Slab1.0: a three-dimensional model of global subduction zone geometries. J. Geophys. Res. 117, B01302. http://dx.doi.org/10.1029/2011JB008524.

Kodaira, S., Takahashi, N., Nakanishi, A., Miura, S., Kaneda, Y., 2000. Subducted seamount imaged in the rupture zone of the 1946 Nankaido earthquake. Science 289, 104–106.

Kopp, H., Kukowski, N., 2003. Backstop geometry and accretionary mechanics of the Sunda margin. Tectonics 22 (6), 1072. http://dx.doi.org/10.1029/2002TC001420.

Krabbenhoeft, A., Weinrebe, R.W., Kopp, H., Flueh, E.R., Ladage, S., Papenberg, C., Planert, L., Djajadihardja, Y., 2010. Bathymetry of the Indonesian Sunda margin-relating morphological features of the upper plate slopes to the location and extent of the seismogenic zone. Nat. Hazards Earth Syst. Sci. 10 (9), 1899–1911. http://dx.doi.org/10.5194/nhess-10-1899-2010.

Lallemand, S.E., Schnurle, P., Malavieille, J., 1994. Coulomb theory applied to accretionary and nonaccretionary wedges—possible causes for tectonic erosion and/or frontal accretion. J. Geophys. Res. 99, 12,033–12,055.

Lay, T., Yue, H., Brodsky, E.E., An, C., 2014. The 1 April 2014 Iquique, Chile, Mw 8.1 earthquake rupture sequence. Geophys. Res. Lett. 41, 3818–3825. http://dx.doi.org/10.1002/2014GL060238.

MacKay, M.E., 1995. Structural variation and landward vergence at the toe of the Oregon accretionary prism. Tectonics 14, 1309–1320.

Maksymowicz, A., 2013. Reestablishment of an accretionary prism after the subduction of a spreading ridge-constraints by a geometric model for the Golfo de Penas, Chile. Geo-Mar. Lett. 33 (5), 345–355. http://dx.doi.org/10.1007/s00367-013-0331-5.

Maksymowicz, A., Contreras-Reyes, E., Grevemeyer, I., Flueh, E.R., 2012. Structure and geodynamics of the post-collision zone between the Nazca–Antarctic spreading center and South America. Earth Planet. Sci. Lett. 345-348, 27–37. http://dx.doi.org/10.1016/j.epsl.2012.06.023.

Maksymowicz, A., Tréhu, A., Conterras-Reyes, E., Ruiz, S., 2015. Density-depth model of the continental wedge at the maximum slip segment of the Maule Mw8.8 megathrust earthquake. Earth Planet. Sci. Lett. 409, 265–277. http://dx.doi.org/10.1016/j.epsl.2014.11.005.

Moreno, M.S., Bolte, J., Klotz, J., Melnick, D., 2009. Impact of megathrust geometry on inversion of coseismic slip from geodetic data: application to the 1960 Chile earthquake. Geophys. Res. Lett. 36. http://dx.doi.org/10.1029/2009GL039276.

Moreno, M., Melnick, D., Rosenau, M., Báez, J.C., Klotz, J., Oncken, O., Tassara, A., Bataille, K., Chen, J., Socquet, A., Bevis, M., Bolte, J., Vigny, C., Brooks, B., Ryder, I., Grund, V., Smalley, R., Carrizo, D., Bartsch, M., Hase, H., 2012. Toward understanding tectonic control on the Mw 8.8, Maule Chile earthquake. Earth Planet. Sci. Lett. 321, 152–165.

Moscoso, E., Grevemeyer, I., Contreras-Reyes, E., Flueh, E.R., Dzierma, Y., Rabbel, W., Thorwart, M., 2011. Revealing the deep structure and rupture plane of the 2010 Maule, Chile earthquake (Mw = 8.8) using wide angle seismic data. Earth Planet. Sci. Lett. 307, 147–155. http://dx.doi.org/10.1016/j.epsl.2011.04.025.

Müller, R.D., Sdrolias, M., Gaina, C., Roest, W.R., 2008. Age, spreading rates, and spreading asymmetry of the world's ocean crust. Geochem. Geophys. Geosyst. 9, Q04006. http://dx.doi.org/10.1029/2007GC001743.

Park, J.T., Tsuru, Y., Kaneda, Y., Kono, S., Kodaira, N., Takahashi, N., Kinoshita, H., 1999. A subducting seamount beneath the Nankai Accretionary Prism off Shikoku, southwestern Japan. Geophys. Res. Lett. (ISSN: 0094-8276) 26. http://dx.doi.org/10.1029/1999GL900134.

Polonia, A., Torelli, L., Brancolini, G., Loreto, M.F., 2007. Tectonic accretion versus erosion along the southern Chile trench: oblique subduction and margin segmentation. Tectonics 26, TC3005. http://dx.doi.org/10.1029/2006TC001983.

Rabus, B., Eineder, M., Roth, A., Bamler, R., 2003. The shuttle radar topography mission- a new class of digital elevation models acquired by spaceborne radar. ISPRS J. Photogramm. Remote Sens. 57, 241–262.

Ranero, C.R., von Huene, R., Weinrebe, W., Reichert, C., 2006. Tectonic processes along the Chile convergent margin. In: Onken, O., et al. (Eds.), The Andes: Active Subduction Orogeny. Springer-Verlag, Berlin, pp. 91–122.

Ruegg, J.C., Rudloff, A., Vigny, C., Madariaga, R., de Chabalier, J.B., Campos, J., Kausel, E., Barrientos, S., Dimitrov, D., 2009. Interseismic strain accumulation measured by GPS in the seismic gap between Constitución and Concepción in Chile. Phys. Earth Planet. Inter. 175, 78–85. http://dx.doi.org/10.1016/j.pepi.2008.02.015.

Ruh, J., Gerya, T., Burg, J.P., 2013. High resolution 3D numerical modeling of thrust wedges: Influence of décollement strength on transfer zones. Geochem. Geophys. Geosyst. 14 (4), 1131–1155.

Sallares, V., Ranero, C.R., 2005. Structure and tectonics of the erosional convergent margin off Antofagasta, north Chile (23°30′S). J. Geophys. Res. 110, B06101.

Scherwath, M., Contreras-Reyes, E., Flueh, E.R., Grevemeyer, I., Krabbenhoeft, A., Papenberg, C., Petersen, C.J., Weinrebe, R.W., 2009. Deep lithospheric structures along the southern central Chile margin from wide-angle P-wave modelling. Geophys. J. Int. 179 (1), 579–600. http://dx.doi.org/10.1111/j.1365-246X.2009.04298.x.

Simpson, G.D.H., 2010. Formation of accretionary prisms influenced by sediment subduction and supplied by sediments from adjacent continents. Geology 38 (2), 131–134.

Thomas, T., Livermore, R.A., Pollitz, F., 2003. Motion of the Scotia Sea plates. Geophys. J. Int. 155, 789–804.

Thornburg, T.M., Kulm, L.D., 1987. Sedimentation in the Chile Trench: depositional morphologies, lithofacies, and stratigraphy. Geol. Soc. Am. Bull. 98, 33–52.

Völker, D., Geersen, J., Contreras-Reyes, E., Reichert, C., 2013. Sedimentary fill of the Chile Trench (32°–46°S): volumetric distribution and causal factors. J. Geol. Soc. Lond. http://dx.doi.org/10.1144/jgs2012-119.

Wang, K., Hu, Y., 2006. Accretionary prisms in subduction earthquake cycles: The theory of dynamic Coulomb wedge. J. Geophys. Res. 111, B06410. http://dx.doi.org/10.1029/2005JB004094.

Wells, R.E., Blakely, R.J., Sugiyama, Y., Scholl, D.W., Dinterman, P.A., 2003. Basin-centered asperities in great subduction zone earthquakes: a link between slip, subsidence, and subduction erosion? J. Geophys. Res. 108, 2507. http://dx.doi.org/10.1029/2002JB002072 (B10).

Zelt, C.A., 1999. Modelling strategies and model assessment for wide-angle seismic travel time data. Geophys. J. Int. 139, 183–204.

Zhao, W., Davis, D.M., Dahlen, F.A., Suppe, J., 1986. Origin of convex accretionary wedges: evidence from Barbados. J. Geophys. Res. (ISSN: 0148-0227) 91. http://dx.doi.org/10.1029/0JGREA000091000B10010246000001.